Explicitly Resolving Lightning and Electrification Processes from the 10-12 April 2019 Thundersnow Outbreak

Sebastian S. Harkema[1†], Edward R. Mansell[2], Alexandre O. Fierro[3], Lawrence D. Carey[4], Christopher J. Schultz[5], Toshi Matsui[6,7], Emily B. Berndt[5]

[1]Earth System Science Center, University of Alabama in Huntsville, Huntsville, AL

[2]NOAA/National Severe Storms Laboratory, Norman, OK

[3]Metocean Team, I&E Engineering, BP Exploration and Operating Company, Ltd., Sunbury, United Kingdom

[4]Department of Atmospheric and Earth Science, University of Alabama in Huntsville, Huntsville, AL

[5]Earth Science Branch, NASA Marshall Space Flight Center, Huntsville, AL

[6]Mesoscale Atmospheric Processes Laboratory, NASA Goddard Space Flight Center, Greenbelt, MD

[7]Earth System Science Interdisciplinary Center, University of Maryland, College Park, MD

Corresponding author: Sebastian Harkema (sebastian.harkema@nasa.gov)

[†]Corresponding author address: Earth System Science Center, University of Alabama in Huntsville, 320 Sparkman Dr. NW, Huntsville, AL 35899

Key Points:

- Model simulated lightning within snowfall (i.e., thundersnow) was compared to ground- and space-based lightning observations
- Thundersnow flashes were initiated in elevated convection that traversed isentropically and were spatially offset from the synoptic snowband
- A conceptual model was developed to explain why thundersnow was spatially offset from the largest reflectivity cores within the snowband

Abstract

The 10-12 April 2019 thundersnow (i.e., lightning within snowfall) outbreak was examined via ground- and space-based lightning observations and was simulated using a numerical weather prediction model with an explicit electrification parameterization. When compared to observations, the simulation propagated the synoptic snowband two to six hours faster while also exaggerating the 3-D reflectivity structure. Throughout the event, the simulation produced 1,733 thundersnow flashes which was less than what was observed by ground- and space-based lightning sensors. In general, simulated thundersnow flashes were spatially offset from the largest reflectivities within the synoptic snowband and tended to occur within elevated convection that traversed isentropically along the top of mid-level frontogenesis. These simulated thundersnow flashes were associated with a tripole charge structure with ice/snow hydrometeors contributing most to the main negative charge region. Both simulated and observed thundersnow flashes initiated in conditionally unstable environments. Lastly, a conceptual model was developed to explain the spatial separation between the largest reflectivities in the snowband and the occurrence of thundersnow. It is hypothesized that the spatial offset of thundersnow initiation from the reflectivity cores within the synoptic snowband arose from a thermal circulation – induced by mid-level frontogenesis – that advects positively charged ice/snow hydrometeors towards the surface and creates a nearly homogeneous vertical charge structure.

Plain Language Summary

The 10-12 April 2019 thundersnow event was examined using lightning observations and a numerical simulation. Both observed and simulated thundersnow flashes occurred in slightly unstable environments in the presence of small ice pellets in elevated convection. The charge on the ice and snow hydrometeors slightly offset the charge on the small ice pellets in the cloud

structure. Simulated thundersnow flashes also occurred away from the heaviest snowfall rates at the surface. This is a result of a vertical air circulation in the environment that transports positively charged ice/snow hydrometeors downward and prevents thundersnow from occurring in the heaviest surface snowfall rates.

1 Introduction

A long history of in situ measurements and laboratory studies led to a consensus that non-inductive collisional ice charging remains the primary mechanism for charge generation within mixed phase clouds (Reynolds et al., 1957; Saunders et al., 2006; Takahashi, 1978). More specifically, non-inductive charging results from the rebounding collisions of graupel and ice crystals in the presence of supercooled liquid water. Hydrometeor sedimentation separates the charged hydrometeors over the scale of the cloud and creates distinctive regions with net charge (e.g., tripole; Williams, 1989). This cloud-scale charge separation generates electric fields (**E**), which, when large enough, initiate lightning discharges (i.e., lightning initiation; MacGorman et al., 2001).

Several studies have used numerical weather prediction models to augment our understanding of small-scale, explicit in-cloud electrification processes and lightning initiation/propagation (e.g., Mansell et al., 2005). Fierro et al., (2013) implemented an explicit electrification parameterization within the Weather Research and Forecasting – Advanced Research WRF dynamical core (WRF-ARW; Skamarock & Klemp, 2008) framework, referred to as WRF-ELEC. WRF-ELEC follows the fundamental principles of electrification and incorporates both non-inductive and inductive charging mechanisms within a bulk microphysics scheme. More specifically, WRF-ELEC operates in the following order: 1) Calculates charge transfer rate via rebounding collisions, 2) Calculates charge density, 3) Determines the 3-D ambient electric potential and **E**, 4) Produces a lightning discharge (if any) and 5) Reduces hydrometeor charge (superposition) within lightning flash volumes. Fierro et al., (2013) highlighted the realism of WRF-ELEC by simulating three different cases: a continental squall line, a major hurricane, and a winter storm. Overall, the simulated spatial extent of the flashes matched qualitatively well with ground-based lightning observations. Their modeled winter storm system did not generate appreciable E (i.e., < 50 V m^{-1}) and, as a result, no lightning discharge were simulated. Dafis et al., (2018) used WRF-ELEC to quantitatively examine several lightning producing cases over Greece and showed that WRF-ELEC was able to reasonably reproduce the bulk of the observed lightning locations and rates. Schultz et al., (2021) used **E** measurements above non-lightning producing snowstorms and demonstrated that weak electrification was possible in these wintertime environments. Using the NASA Unified WRF with electrification parameterization (NU-WRF-ELEC; Fierro et al., 2013; Peters-Lidard et al., 2015; Skamarock & Klemp, 2008), Harkema et al., (2023) simulated two snowstorms sampled during the NASA Investigation of Microphysics and Precipitation for Atlantic Coast-Threatening Snowstorms (IMPACTS; McMurdie et al., 2022) field campaign. Although neither simulation produced lightning discharges within snowfall, the simulations did produce appreciable **E** in the snowstorms (i.e., 11.7 and 18.3 kV m^{-1}, respectively); representing, to the authors knowledge, an initial effort demonstrating the capability of cloud-scale electrification models to simulate strong **E** within synoptic-scale snowstorms.

Studies have examined the electrification process and lightning initiation within snowfall (i.e., thundersnow) via in-situ measurements (Kitagawa & Michimoto, 1994; Rust & Trapp, 2002), ground- (Adhikari & Liu, 2019; Kumjian & Deierling, 2015; Rauber et al., 2014; Schultz et al., 2018), and space-based lightning observations (Harkema et al., 2019, 2020, 2022). Lightning should ideally be studied via all available observational means/platforms as each lightning observing system complements the other. For example, space-based lightning observations provide insight on flash size but not flash type; in contrast, the most common (i.e., very-low-frequency, VLF) ground-based sensors are able to retrieve flash type and polarity but not flash size. Winter convective storms are associated with a gross tripole charge structure even though they are shallower than summertime convection (e.g., Krehbiel, 1986). Stratiform regions of winter storms are generally characterized by a positive charge region atop a negative charge region (Rust & Trapp, 2002; Schultz et al., 2018). To better understand the environmental characteristics leading to thundersnow initiation, Curran & Pearson, (1971) examined upper air soundings in proximity to 13 thundersnow events detected by ground-based stations. These 13 thundersnow events were associated with a stable lower troposphere capped with a layer of nearly constant equivalent potential temperature (θ_e). Unfortunately, Curran & Pearson, (1971) did not filter their proximity soundings by the type of event that the thundersnow was associated with (i.e., lake-effect snow, synoptic snowfall, etc.). To address this issue, Market et al., (2006) used ground-based lightning observations to examine proximity soundings for thundering and non-thundering snowfall events for extratropical cyclones in the absence of external forcing (i.e., lake-effect or orographic influences). From this comparison, the mean upper air soundings from the thundersnow cases were statistically different with respect to 1) a lower pressure for the most unstable parcel (about 50 hPa above a frontal inversion at the surface) and 2) mid-level (700-500 hPa) lapse rates being steeper (associated with significant drying above the frontal inversion). Furthermore, they found that the majority of the examined thundersnow events were associated with negligible (i.e., ~0 J kg^{-1}) convective available potential energy (CAPE) values.

Market & Becker, (2009) examined thundersnow flashes – identified via ground observations – with respect to snowband orientation and maximum reflectivity and found that thundersnow was more likely to occur on the leading edge of the snowband and was spatially disjoint from the highest reflectivity values by a mean distance of 17 km. When examining space-based thundersnow flash observations, Harkema et al., (2020) found similar results but with a mean spatial offset from thundersnow and the heaviest surface snowfall rates of about 131±65 km. These spatial offset differences arise from inherent dissimilarities in highest reflectivity in synoptic snowbands (Market & Becker 2009) versus largest derived surface snowfall rates (i.e., ≥ 4.44 cm h^{-1}; Harkema et al., 2020). Furthermore, Harkema et al., (2020) examined isothermal reflectivity (i.e., -10°C, -15°C, and -20°C) for 339 ground-based identified thundersnow flashes from 13 April 2018 and determined that maximum and mean isothermal reflectivity values were < 30 and < 23 dBZ (for all three temperatures), respectively. As a result, the isothermal reflectivity in winter storms associated with lightning were slightly lower compared to those for lightning initiation in summertime convection (e.g., Mosier et al., 2011; Seroka et al., 2012). Overall, these studies provide context to the physical processes that are involved within the cloud structure that could lead to thundersnow initiation.

The demonstration of using NU-WRF-ELEC to successfully simulate electrification processes within non-lightning producing winter storms provides the initial step to explicitly resolve thundersnow (i.e., Harkema et al., 2023). The chief goal of this work is to address the following questions: 1) Is it possible for NU-WRF-ELEC to produce enough charge separation during a snowstorm to explicitly produce a lightning discharge in snowfall? 2) How well do simulated thundersnow flashes compare to ground- and space-based lightning observations? 3) Do the simulated electrical properties (e.g., charge structure) associated with regions of thundersnow match those from previous observational studies? In summary, the objectives of this manuscript are:

1) Simulate the 10-12 April 2019 extratropical cyclone thundersnow outbreak that occurred in the northern Great Plains of the United States using NU-WRF-ELEC and the branching volume lightning discharge scheme (MacGorman et al., 2001);

2) Compare the horizontal spatial extent and other characteristics of simulated thundersnow flashes with available ground- and space-based lightning observations;

3) Quantitatively analyze the charge on individual hydrometeor types, charge structure, and reflectivity characteristics of regions of simulated thundersnow.

2 Data and Methods

2.1 10-12 April 2019 Thundersnow Outbreak Event Overview

Between 10-12 April 2019, a heavy-banded snowfall event produced a large swath of heavy snowfall to much of the northern Great Plains of the United States with some areas receiving more than 60 cm (~2 feet) of snowfall (Fig. 1). The surface low pressure developed on the leeside of the Rocky Mountains in Colorado and Wyoming on 10 April 2019. The cyclone of 986 hPa traversed south into Kansas on 11 April 2019 before propagating northward. The system became vertically stacked along the Minnesota and Iowa border around 12 UTC on 12 April 2019 (994 hPa). Throughout the duration of the event, surface snowfall rates exceeded 2.54 cm h^{-1} (1 in h^{-1}) and thundersnow was frequently observed from ground- and space-based lightning detection systems. Nearly 20,000 thundersnow flashes were observed from the Geostationary Operational Environmental Satellite-16 Geostationary Lightning Mapper (GLM; Goodman et al., 2013; Rudlosky et al., 2019) and more details regarding these thundersnow flashes can be found in section 2.3. As a result, the 10-12 April 2019 thundersnow outbreak event was an ideal case to simulate with NU-WRF-ELEC.

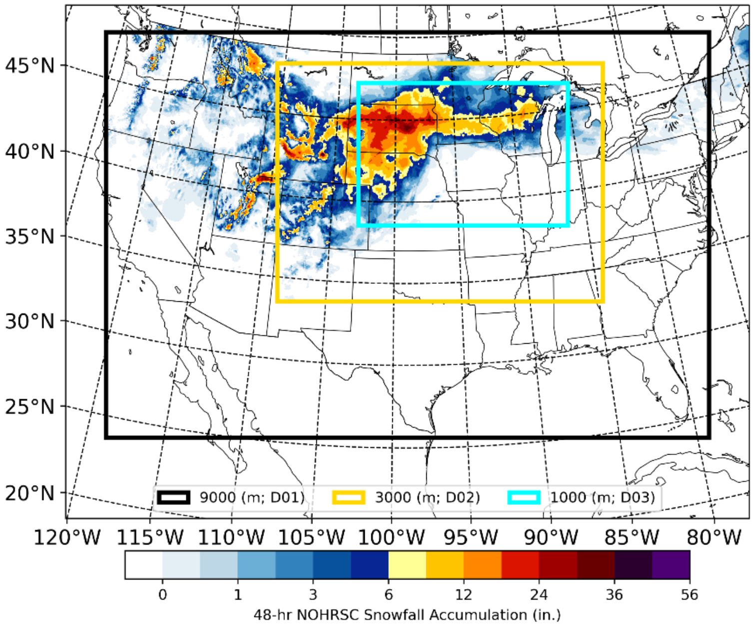

Figure 1: NU-WRF-ELEC spatial domains and 48-hour National Operational Hydrologic Remote Sensing Center snowfall accumulation ending at 00 UTC on 12 April 2019.

2.2. NASA Unified Weather Research and Forecasting with Electrification

Except from the lightning discharge parameterization, the parameterization setup for this study was identical to that of the NU-WRF-ELEC simulations in (Harkema et al., 2023). Specifically, a more complex lightning branching volume discharge scheme (Fierro et al., 2015; MacGorman et al., 2001) was utilized as it is more representative of the horizontal spatial extent of lightning than the simple bulk cylindrical lightning discharge scheme (Ziegler & MacGorman, 1994). Essentially, in the bulk scheme, if the maximum **E** profile (e.g., Dwyer, 2003) exceeds the breakdown initiation threshold (e.g., 120 kV m^{-1}) a lightning discharge is produced. The parameterized lightning channel volumes deposit charge on the hydrometeors (via superposition). One benefit of using the more complex volume lightning discharge scheme in WRF-ELEC is that the parameterization provides an estimate of intracloud (IC) and cloud-to-ground (CG) flashes (e.g., Fierro et al. 2015).

The NU-WRF-ELEC simulation contains two nested domains with the innermost domain being centered over the Iowa/Minnesota border (Fig. 1). Table 1 contains the summary of the parameterizations and grid specs for the three domains of the NU-WRF-ELEC simulation. The operational High-Resolution Rapid Refresh (HRRR; Benjamin et al., 2016) model provided the boundary conditions for the NU-WRF-ELEC simulation. More specifically, hourly HRRR analysis data (not forecast data) between 00 UTC 8 April 2019 and 06 UTC 12 April 2019 provide the lateral boundary conditions. The NU-WRF-ELEC simulation used the National Severe Storms Laboratory (NSSL) two-moment bulk microphysics scheme (Mansell et al., 2010) which predicts the mass mixing ratio and number concentrations for hydrometeors (e.g., ice crystals, snow, graupel, hail, droplets, and rain). Shortwave and longwave radiation were parameterized using the Rapid Radiative Transfer Model for General Circulation Models (RRTMG; Iacono et al., 2008). The Yonsei University (YSU) planetary boundary layer scheme was used to parameterize the subgrid-scale turbulent processes within the boundary layer (Noh et al., 2003). The Unified Noah land surface model (Ek et al., 2003) was used to facilitate the conditions for turbulent surface fluxes. The Kain-Fritsch subgrid convective parameterization scheme (Kain et al., 2006) was used to assist with the convective processes for domains with a grid spacing greater than 3 km (i.e., outer domain only; Fig. 1). It should also be noted that data assimilation was not performed.

Parameters	D01	D02	D03
Start Datetime	00 UTC 08 April 2019	00 UTC 09 April 2019	00 UTC 10 April 2019
End Datetime	06 UTC 12 April 2019	06 UTC 12 April 2019	06 UTC 12 April 2019
ΔX (m)	9000	3000	1000
N_Z	70	70	70
N_X x N_Y	457 x 307	739 x 541	1426 x 973
dt (s)	10	5	5
Boundary Layer Scheme	YSU	YSU	YSU
Radiation Scheme	RRTMG	RRTMG	RRTMG
Microphysics Scheme	NSSL two-moment	NSSL two-moment	NSSL two-moment
Land Surface Model	Noah	Noah	Noah
Initial-Boundary Conditions	HRRR analysis (v3)	HRRR analysis (v3)	HRRR analysis (v3)

Table 1: Summary of key physical and numerical parameterizations of the three domains of the NU-WRF-ELEC simulation. The variables ΔX, N_Z, N_X x N_Y, and dt are the horizontal grid spacing, number of vertical layers, number of grid points in the zonal and meridional directions, and computational time step, respectively.

WRF-ELEC calculates the charge transfer rates between rebounding collisions of hydrometeor species within the NSSL microphysics scheme (i.e., droplets, rain, ice crystals, snow, graupel, and hail). Both inductive and non-inductive charging mechanisms were parameterized within the simulation (Mansell et al., 2005, 2010; Saunders & Peck, 1998). From here, WRF-ELEC determines the net charge changes from the mass and charge transfer processes and follows the conservation of mass and charge. The space charge follows the hydrometeors around and thus sedimentation and advection of charge is identical to other scalar variables. The electric potential (ϕ) is then calculated by solving the Poisson equation (Eq. 1):

$$\nabla^2\phi = -\frac{\rho_{tot}}{\epsilon} \quad (1)$$

where ρ_{tot} is the net space charge within the gridcell, and ϵ is the electric permittivity of air (i.e., 8.85x10^{-12} F m^{-1}). Once electric potential is determined, the three components of **E** magnitude are computed via (Eq. 2):

$$\mathbf{E} = -\nabla\phi \quad (2)$$

where **E** is equal to the negative gradient of electric potential. Specifically for this study, an electrical screening layer parameterization was applied to all cloud/clear air boundaries (Ziegler et al., 1991) to approximate the effects of clean-air ion currents, resulting in charge attachment to cloud-edge hydrometeors. Screening layers reduce E caused by charges within the cloud in clear air, particularly above cloud top. It should be noted that the screening layer parameterization does not conserve charge, which otherwise would require small ion physics (attachment and Brownian drift, Chiu 1978) that are not yet included in WRF-ELEC.

2.3 Defining Thundersnow and Lightning Dataset

Using the thundersnow detection algorithm (Harkema et al., 2019, 2020, 2022), 19,677 flashes observed by the GLM were classified as thundersnow within the geographical region bounded by the NU-WRF inner-most domain– from 10-12 April 2019 – and gridded using the GLMTools Python software (Bruning et al., 2019). This thundersnow detection algorithm objectively identifies thundersnow flashes by finding the spatial and temporal coincidence of GLM data and derived snowfall rates from the merged snowfall rate product (Meng, et al., 2017; Meng et al., 2017). It should be mentioned that the ground-based radar data in the merged snowfall rate product classifies snowfall at a location where the temperature and wet-bulb temperature are below

2°C and 0°C, respectively. A complete description of the thundersnow detection algorithm can be found in Harkema et al. (2019). Specifically, this study used level 2 data, minimum flash area (MFA), and flash extent density (FED) gridded data from GLM-East as it was more suitable for validation of potential thundersnow lightning discharges from NU-WRF-ELEC in the central and eastern United States (Rudlosky & Virts, 2021). The National Lightning Detection Network (NLDN; Cummins & Murphy, 2009) and the Earth Networks Total Lightning Network (ENTLN; Liu & Heckman, 2010) flash data were matched up with thundersnow flashes observed by the GLM using the ±1-second and 50-km distance threshold from Harkema et al., (2019). As a result, 39,564 NLDN flashes and 144,198 ENTLN flashes were objectively classified as thundersnow. ENLTN operates at a larger frequency range compared to NLDN (1 Hz to 12 MHz versus 400 Hz to 400 kHz) and therefore can observe and classify more lightning flashes (Cummins & Murphy, 2009; Liu & Heckman, 2010). Additionally, ENTLN data does not cover the entire duration of the event as several hours of data were missing after 22 UTC on 11 April 2019. It should also be noted that a single GLM flash can consist of multiple ground-based lightning flashes (e.g., Harkema et al., 2019; Lyons et al., 2020). GLM, NLDN, and ENTLN data were used for NU-WRF-ELEC lightning discharge validation. Furthermore, NU-WRF-ELEC thundersnow flashes were defined as a clustered lightning discharge that were collocated with a surface temperature and wet-bulb temperature ≤ 2°C. More specifically, only a portion of the clustered lightning discharge had to meet these criteria. This definition is similar to how thundersnow flashes were identified and classified in Harkema et al., (2019, 2020, 2022). As a result of this definition, multiple simulated lightning initiation points may have occurred within a clustered lightning discharge.

2.4 Multi-Radar Multi-Sensor Reflectivity Comparison

The Multi-Radar Multi-Sensor (MRMS; Smith et al., 2016) analysis system provides a high spatial resolution (1 km x 1 km) 3-D radar mosaic product in two-minute intervals at several height levels above mean sea level throughout the CONUS. MRMS also provides isothermal reflectivity values at 5°C intervals between 0°C and -20°C. This study used both the 3-D and isothermal reflectivity data for validating NU-WRF-ELEC simulation output and to provide context to the processes associated with observed thundersnow initiation. More specifically, simulated and observed 3-D reflectivity structures were examined via contour frequency by altitude diagram (CFAD) scores (CS_h; Nicholls et al., 2017) which compare the probability density functions (PDFs) of the observed and simulated reflectivity at individual heights:

$$CS_h = 1 - \frac{\sum |PDF_m - PDF_o|_h}{200} \quad (3)$$

In Eq. 3, CS_h is the CFAD score at a specific height, PDF_m and PDF_o (%) are the PDFs at constant heights for modeled and observed reflectivity, respectively, and the 200 in the denominator is a normalization factor. The CS_h value ranges from 0 (no agreement) to 1 (complete agreement) between NU-WRF-ELEC and MRMS reflectivity PDFs at a specific height. One benefit of using

CS_h is that it is insensitive to any spatiotemporal errors with the model compared to observations (Lang et al., 2014; Nicholls et al., 2017; Yuter & Houze, 1995).

3 Analysis

3.1 Radar Reflectivity Analysis

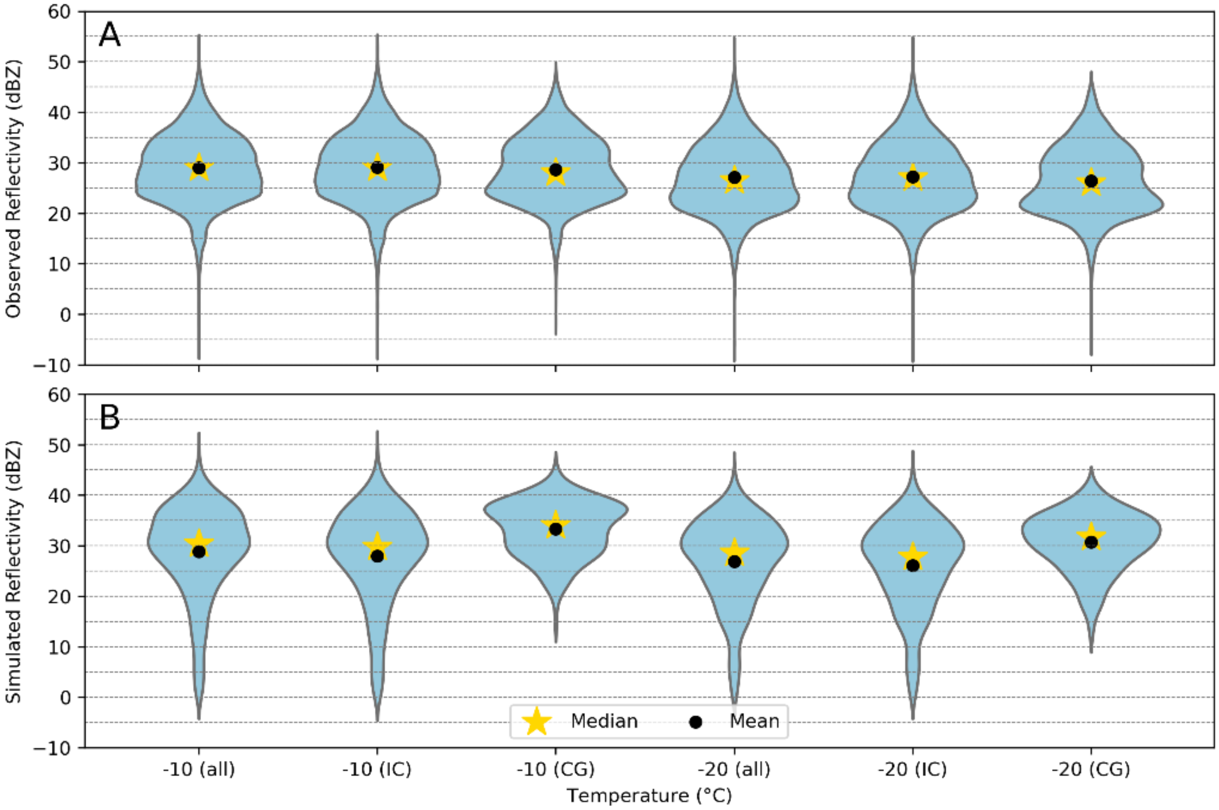

Figure 2: Violin plots of -10°C and -20°C isothermal reflectivities for: A) 26,953 NLDN observed thundersnow flashes and B) 1,195 simulated thundersnow flashes between 00 and 16 UTC on 11 April 2019. During this period, NLDN detected 4,166 CG and 22,787 IC thundersnow flashes while NU-WRF-ELEC simulated 205 CG and 990 IC thundersnow flashes.

Between 00 and 16 UTC on 11 April 2019 and within the spatial extent of the inner-most domain of the NU-WRF simulation, the NLDN detected 26,953 thundersnow flashes while NU-WRF-ELEC simulated 1,195 individual thundersnow flash footprints. All individual thundersnow flash footprints were associated with some solid precipitation (i.e., snow and/or graupel) at or near the surface. This may also indicate the location was experiencing mixed-phase precipitation and provides evidence that the temperature and wet-bulb temperature criteria performs well in defining simulated flash clusters as thundersnow. The observed NLDN thundersnow flashes were matched up with the nearest MRMS -10°C and -20°C isothermal reflectivity data (Fig. 2a). At both isothermal levels (i.e., -10°C and -20°C), the overall NLDN thundersnow distributions were similar to the distributions when only considering IC flashes (Fig. 2a). This is not surprising as the vast majority of NLDN thundersnow flashes were classified as ICs. In contrast, when only CG thundersnow flashes were examined, both isothermal levels were associated with a slight bimodality and lower reflectivity compared to IC thundersnow (Fig. 2a). For example, the mode reflectivity – at both isothermal levels – were at least 2 dBZ lower for CG thundersnow compared to IC thundersnow. In contrast, the simulated reflectivity values were interpolated to the isothermal levels using MetPy (May et al., 2022; Fig. 2b). It should be noted that vertical profiles of simulated thundersnow flashes were all based on mean values within the simulated flash footprints. In general, NU-WRF-ELEC tended to overestimate the isothermal reflectivity in regions associated with thundersnow compared to observations especially for CGs (Fig. 2).

Although isothermal reflectivity has been shown to be a potential indicator for lightning initiation (e.g., Mosier et al. 2011; Seroka et al. 2012), it does not provide complete context to the actual vertical distribution of hydrometeors. To address this, Figure 3 displays the vertical reflectivity distributions (e.g., height above mean sea level) associated with the simulated thundersnow flashes (N = 1,195) and observed thundersnow flashes via NLDN (N = 26,953) that occurred between 00 and 16 UTC on 11 April 2019. The shading represents one standard deviation away from the mean vertical reflectivity profile (solid lines; Fig. 3). Like in Fig. 2, the reflectivity distributions for all flashes and IC flashes were more comparable to each other than the CG flashes (Fig. 3). Again, this results from the fact that the majority of thundersnow flashes were classified as ICs. In fact, the CS_h values associated with thundersnow regions exceeded 0.7 throughout the lowest 9 km of the vertical profile (Fig. 3a,b). In contrast, the CS_h values for the CG distribution remained below 0.7 at 2640+ m above mean sea level (Fig. 3c). Similar to Fig. 2, the simulation indicated that the mean vertical reflectivities for CGs flashes were larger compared to IC flashes (Fig. 3b,c). More specifically, the mean reflectivity profile for CGs exceed 30 dBZ between 1,000 m and 6,100 m above mean sea level; the mean reflectivity profile for ICs never exceeded 28 dBZ. Simulated CGs occurred throughout the synoptic snowband and yet did not occur in more convective regions compared to simulated ICs (not shown). As a result, the differences between the CG and IC simulated vertical reflectivity profiles was likely a result of simulated CG flashes occurring in regions associated with larger rates of aggregation throughout the vertical profile. For example, chain-like aggregation has been shown to be associated with regions of enhanced electrification (e.g., Dye & Bansemer, 2019; Stith et al., 2002). In general, aggregation increases hydrometeor size and results in higher radar reflectivity (i.e., $Z \alpha D^6$). Thus, this is a direct result of the NSSL microphysics scheme being too aggressive with the aggregation parameterization (e.g., Fierro et al. 2015). When examining all thundersnow flashes, the highest CS_h of 0.87 occurred at a height of 3km (Fig. 3a).

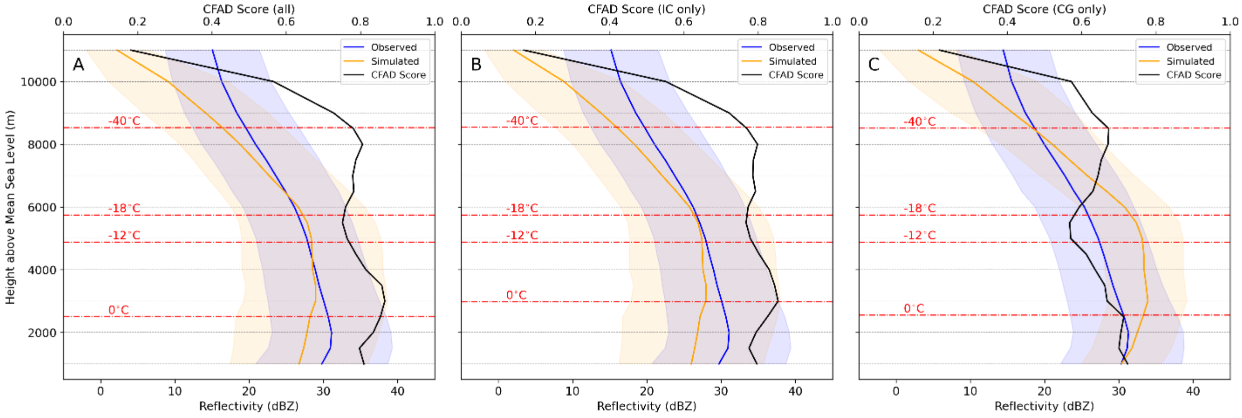

Figure 3: Mean vertical reflectivity structure with standard deviation shaded between 00 and 16 UTC on 11 April 2019: A) NLDN observed (blue; 26,953) and simulated (orange; N = 1,195) for CG and IC thundersnow flashes, B) NLDN observed (blue; 22,787) and simulated (orange; N = 990) for CG thundersnow flashes C) NLDN observed (blue; 4,166) and simulated (orange; N = 205) for CG thundersnow flashes. The black line is the calculated contour frequency by altitude diagram score that compares the probability density functions of the reflectivity structure of the observed and simulated thundersnow flashes. The horizontal red dashed lines represent specific mean simulated temperature levels for the subset of thundersnow flashes.

The simulation and observed reflectivities throughout the inner-most domain were also compared - at hourly intervals - between 15 UTC on 10 April 2019 and 04 UTC on 12 April 2019 (i.e., when MRMS 3-D reflectivity data was available). The best period of overlap between the two PDFs occurred on 06 UTC on 11 April 2019 with a maximum CS_h value of 0.49 at 2500 m above mean sea level (not shown). This quantitatively demonstrates that the simulation did not do well simulating the reflectivity structures compared to observed MRMS reflectivity (Supplemental

Material 1). More specifically, the simulation exaggerated the reflectivity structure within the synoptic scale snowband. This is not entirely unexpected, as the NSSL microphysics scheme has a known bias with the aggregation parameterization being too aggressive (e.g., Fierro et al. 2015). As a result, the NSSL microphysics scheme tends to produce larger aggregates and, therefore larger reflectivity values, which partly explains the relatively low CS_h values in the system-wide comparison.

3.2 Simulated Electrification Characteristics

To provide 2-D context to the simulated results, Supplemental Material 1 displays the MRMS composite reflectivity and GLM FED, simulated composite reflectivity, maximum E in the vertical, and simulated lightning FEDs. Throughout the simulation both non-inductive and inductive charging mechanisms played a role in charge generation which varied with time and location (Supplemental Material 2). Figure 4a,b shows cross-sections of simulated reflectivity and total space charge density, respectively, from Northern Iowa to Central Minnesota at 0710 UTC on 11 April 2019. The reflectivity cross-section suggests that elevated convection occurred to the south of the main synoptic snowband with reflectivity values generally less than 45 dBZ (Fig. 4a). The broad stratiform snowband in Minnesota, however, was associated with reflectivity values exceeding 50 dBZ particularly closer to the surface. The total space charge density cross-section indicated a gross tripole charge structure in the elevated convection regions but was vertically homogenous in polarity within the main synoptic snowband (Fig. 4b). Along the cross-section in Fig. 4c, NU-WRF-ELEC initiated four lightning flashes in elevated convection (200+ km south of the main snowband) with three of these flashes being initiated within the dendritic growth zone (yellow stars with black outline; Fig. 4c). Additionally, numerous lightning channels propagated through the cross-section (Fig. 4c). These lightning channels can be approximated as branches of a simulated lightning flash. Interestingly, the lightning channels closest to the main synoptic snowband were spatially separated from the highest simulated reflectivities at the surface by approximately 20-100 km (Fig. 4a,c). This region was also associated with enhancements of mid-level frontogenesis (purple contours). The elevated convection appeared to traverse along the top of the mid-level frontogenesis; more specifically, the bases of elevated convective cells appeared to traverse the 320 K θ_e istentrope contour near the top of the stable layer closer to the surface (Supplemental Material 3).

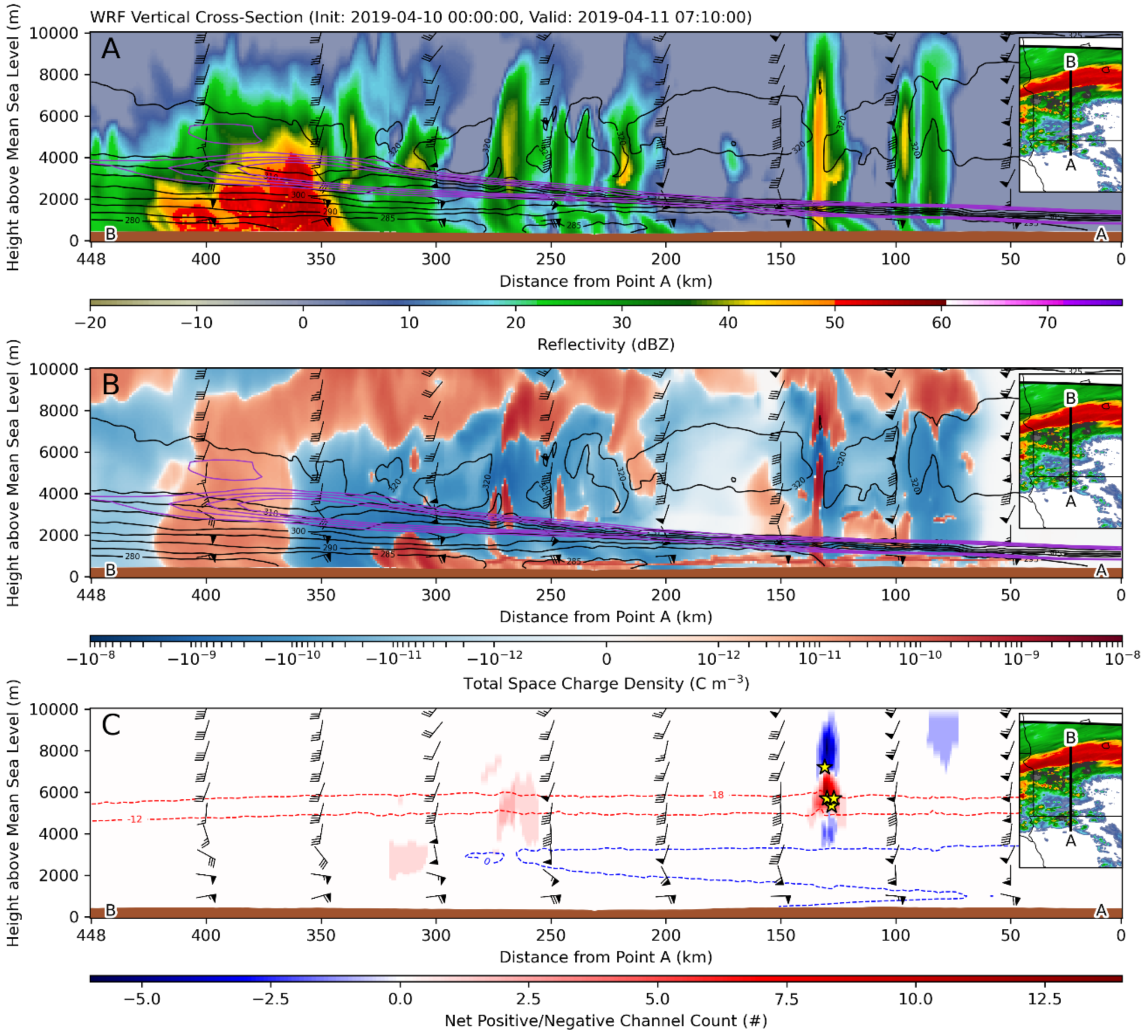

Figure 4: Simulated cross-section from Northern Iowa to Central Minnesota at 0710 UTC on 11 April 2019: A) Simulated reflectivity, B) simulated total space charge density, and C) simulated

net channel count. Panels A) and B) also display contours for frontogenesis (solid purple contours) and θ_e (solid black contours). Panel C) The yellow stars with a black outline are lightning initiation locations. The dashed red and blue lines represent the dendritic growth zone and freezing level, respectively.

Lightning discharges cannot occur without ample charge separation; therefore, it is paramount to understand the vertical charge structure that makes these possible. Overall, NU-WRF-ELEC produced 1,733 clustered lightning flashes that were classified as thundersnow and accounts for 17.3% of the total simulated clustered lightning flashes. The simulated vertical charge structures from all 1,733 simulated thundersnow flashes were statistically analyzed with respect to the six hydrometeors explicitly simulated within the NSSL microphysics scheme (i.e., hail, rain, ice, snow, graupel, and droplets). It was determined that 99.8% of these thundersnow flash clusters were associated with solid precipitation (i.e., snow and/or graupel) at or near the surface (again this may also indicate mixed-phase precipitation). It should be noted that this is not a true analysis of vertical charge structure with height but rather with temperature. As a result, above freezing temperatures were possible and likely associated with warm noses in the thermodynamic profile associated with the surface frontal inversion. The total charge density is the sum of the individual hydrometeor charge densities (Fig. 5). The mean charge density vertical profile (black line) indicates a normal tripole charge structure (Fig. 5a). The mean net charge polarity profile switched from negative to positive at -23°C. Furthermore, the charge density was also associated with variability (i.e., ± one standard deviation; grey shading) resulting from the different vertical profiles that were included. The lower negative and upper positive charge regions were centered near -11°C and -33°C, respectively. As seen in previous modeling studies, the peak negative net charge region was offset from the peak of the negative graupel mean charge density (dashed orange line) and better corresponded to the negative peaks of the mean ice and snow vertical profiles (dashed blue and cyan lines; Fig. 5a), which is the result of the charging history of the hydrometeors. Negative ice/snow from where graupel charges positively is lofted by updrafts and contributes to the lower portion of the net negative charge region (Mansell et al., 2010).

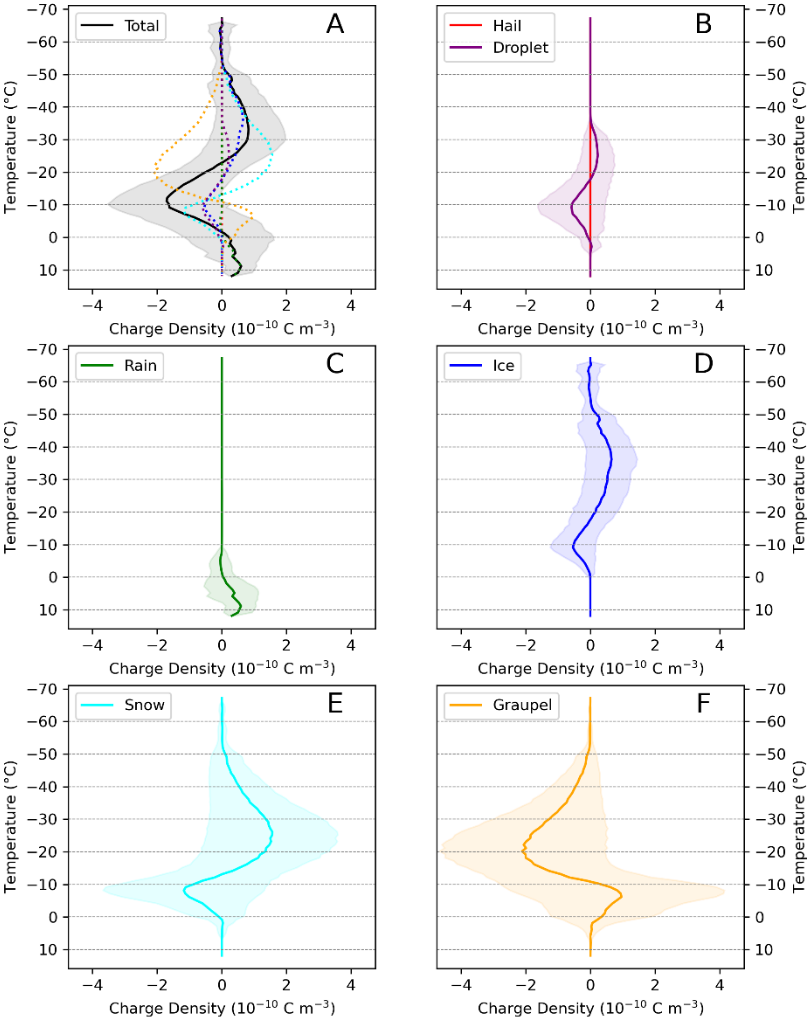

Figure 5: Charge density distributions by temperature for simulated thundersnow locations.

As expected, the hail charge density was several magnitudes lower compared to the other hydrometeors throughout the vertical (Fig. 5b). There should be no appreciable hail mass because there is no wet growth of graupel. The mean charge density for droplet hydrometeors had two peaks centered at -9°C and -25°, respectively (Fig. 5b). Furthermore, the charge density on droplets indicated that droplets warmer than -17°C were more likely to be associated with a negative charge. The largest rain charge density occurred at 9°C (dark green line; Fig. 5b). Positive rain is most likely melted positive graupel. The mean ice charge density (dark blue line; Fig. 5d) was associated with two relative peaks: -9°C and -36°C. Similarly, the mean snow hydrometeor charge density profile contributed to the net mid-level negative charge and the net upper positive charge with peaks at -8°C and -26°C, respectively (Fig. 5a,e). The mean snow charge density polarity reversed at -12°C. Unlike the other hydrometeors, the mean simulated graupel hydrometeor charge density vertical profile had positive and negative charge peaks at -6°C and -20°C, respectively (Fig. 5a,f). Furthermore, the graupel charge density profile indicated that the mean reversal temperature for graupel hydrometeors was -10°C.

3.3 Simulated versus Observed Thundersnow

The thundersnow flashes observed from GLM throughout the event (i.e., between 00 UTC 10 April 2019 and 06 UTC 12 April 2019) were gridded and accumulated throughout this period (Fig. 6a,b). More specifically, Fig. 6a displays the minimum MFA that occurred and Fig. 6b displays the accumulated FED throughout the period. The smallest thundersnow flashes observed by GLM were spatially collocated with the highest observed FED values in Nebraska, South Dakota, and Minnesota. Additionally, there is a secondary FED hotspot in Southern Minnesota that results from a line of elevated convection traversing north from Iowa (Supplemental Material 1). In contrast, GLM observed larger, less-frequent flashes in Wisconsin. Akin to the GLM flashes, NU-WRF-ELEC thundersnow FED values were accumulated over the duration of the simulation (Fig. 6c). The simulation suggested that central Minnesota and eastern South Dakota were associated with the greatest amount of thundersnow, but the spatial extent and magnitude of flashes was less than what GLM observed. The simulation completely misses the thundersnow activity in Southern Minnesota owing to the underperformance of simulated elevated convection in the region. Furthermore, NU-WRF-ELEC simulated thundersnow flashes were smaller than those observed by GLM. The mean (max) NU-WRF-ELEC and GLM thundersnow flash area were 206 km^2 and 514 km^2 (5,142 km^2 and 7,322 km^2), respectively. From a thundersnow flash classification perspective, NLDN and ENTLN detected 26,953 and 115,510 thundersnow flashes, respectively, between 00 UTC and 16 UTC on 11 April 2019. Of those NLDN and ENTLN thundersnow flashes, 15.4% and 13.0% were classified as CGs (Table 2). With regards to CG polarity, 14.7% and 7.3% of CGs identified with NLDN and ENTLN, respectively, were positive. During this same period, NU-WRF-ELEC simulated 2,821 individual thundersnow flashes with 7.5% of simulated CGs being positive (Table 2). The simulation produced a lower relative amount of positive CGs compared to the NLDN.

System	# of ICs	# of CGs	# of Negative CGs	# of Positive CGs
NLDN	22,787	4,166	3,552	614
ENTLN	100,438	15,072	13,975	1,097
NU-WRF-ELEC	2,553	268	248	20

Table 2: NLDN, ENTLN, and NU-WRF-ELEC thundersnow flash classifications between 00 UTC and 16 UTC on 11 April 2019.

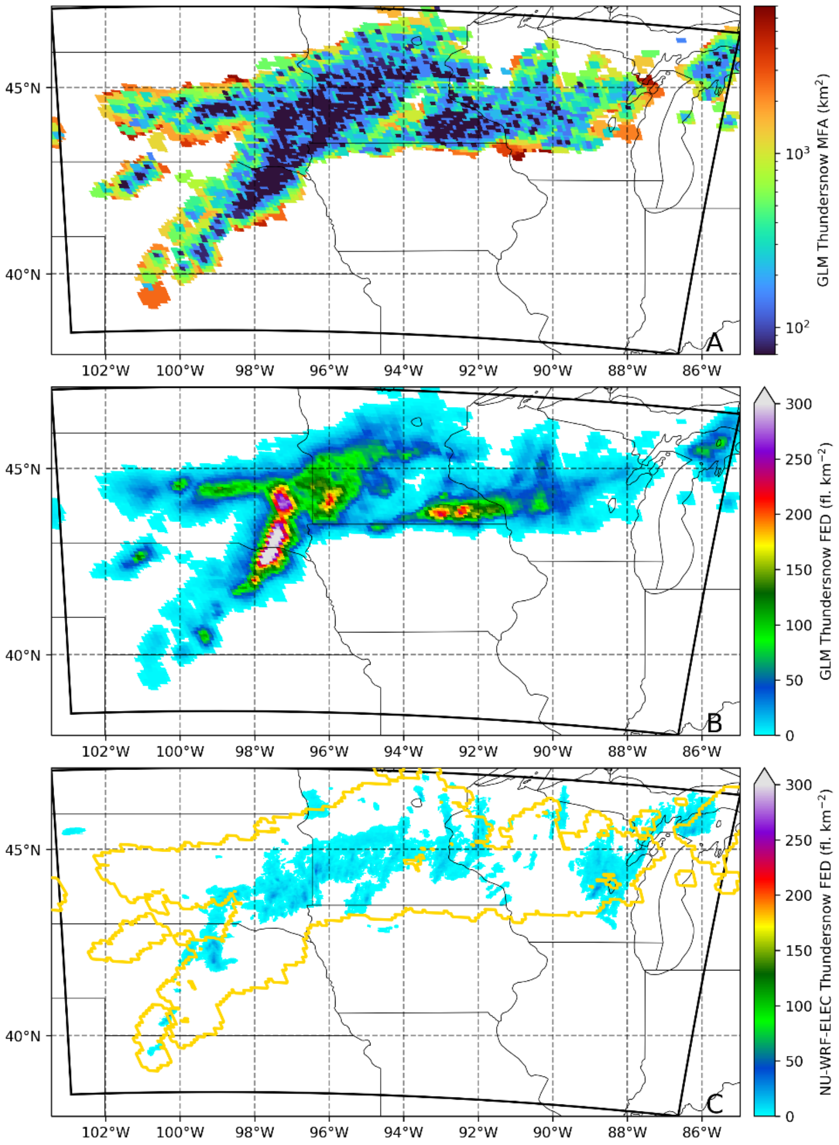

Figure 6: A) Minimum MFA and B) accumulated FED for thundersnow flashes observed by GLM between 00 UTC on 10 April 2019 through 06 UTC 12 April 2019. C) Accumulated FED for simulated thundersnow flashes between 00 UTC 10 April 2019 and 06 UTC 12 April 2019. The gold contour represents the spatial extent of the GLM gridded observations of thundersnow during the same period.

As a result of the previously stated differences between observed and simulated thundersnow, and any potential spatial differences between the two, it becomes paramount to estimate NU-WRF-ELEC lightning discharges and observed lightning relative to one another.

Empirical cumulative density functions provide a means to estimate the relative flash rates of the NU-WRF-ELEC output and lightning observations without considering the flash rate magnitudes and spatial offsets between the data over time. Figure 7 displays the empirical cumulative density functions for NU-WRF-ELEC, GLM, NLDN, and ENTLN between 00 UTC and 16 UTC on 11 April 2019. As expected, the observed thundersnow flashes – from GLM, NLDN, and ENTLN – all follow the same general pattern with respect to time. When the NLDN (orange line) and ENTLN (green line) were to the left of GLM (red line) at an individual time this translated to ground-based networks detecting more individual lightning flashes with respect to GLM. As for NU-WRF-ELEC, the simulation depicted thundersnow on the order of two to six hours ahead of what was observed (solid blue line; Fig. 7). This time discrepancy is associated with the simulation propagating the synoptic snowband too quickly towards northern Minnesota (Supplemental Material 1); which is inherently influenced by the model evolving the upper-level synoptic pattern too quickly. To address this forecast bias in timing, the simulated thundersnow times were adjusted to match the GLM observations to the 10% (dashed blue line) and 50% (dotted blue line) cumulative density function values. These two adjustments indicate slightly different perspectives on how NU-WRF-ELEC simulated thundersnow compared to observations. From the 10% adjustment, the simulation quickly produced more relative thundersnow flashes compared to the observations throughout much the period (i.e., blue dashed line is to the left of the observed lines; Fig. 7). In contrast – with the 50% adjustment – the simulation underestimates the observations throughout the period (i.e., blue dotted line is right of the observed lines; Fig. 7). This 50% adjustment hints that WRF-ELEC has difficulty simulating the electrification processes and lightning production at the beginning and end of this period. This discrepancy can be seen – by focusing on the period between 00 and 16 UTC on 11 April 2019 - in Supplemental Materials 1.

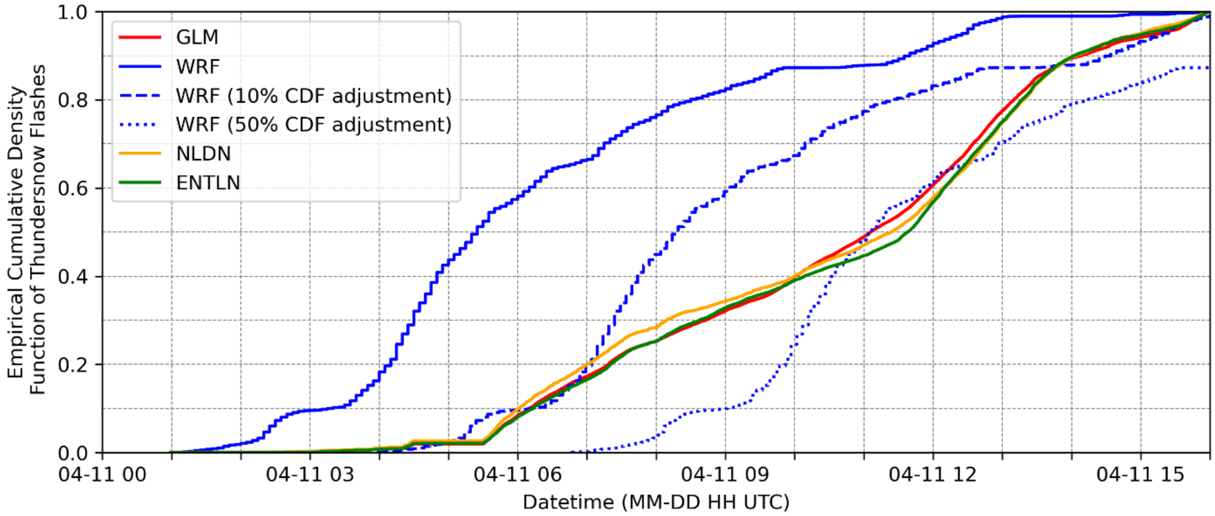

Figure 7: Empirical cumulative density functions for simulated thundersnow flashes (blue) and observed thundersnow flashes from NLDN (orange), ENTLN (green), and GLM (red) between 00 and 16 UTC on 11 April 2019. Adjustments for forecast bias in timing for simulated thundersnow flashes are also shown by 2.9 hours (blue dashed) and 5.7 hours (blue dotted) to match up at 10% and 50% cumulative density function levels, respectively.

3.4 Thermodynamic Characteristics

A composite vertical profile was created using all 1,733 simulated thundersnow flashes to provide additional context to the environment that would be conducive for thundersnow (Fig. 8). The mean thundersnow environment was associated with ice supersaturation as large as 3.5% and was supersaturated with respect to ice between 600 and 370 hPa (Fig. 8a). Upward motions persisted between 820 and 220 hPa and peaked just above the dendritic growth zone (i.e., -6.6 Pa s^{-1} at 475 hPa; Fig. 8a). Furthermore, the mean vertical profile values in the Skew-T *log-p* diagram indicate the environment was associated with a large frontal inversion below 700 hPa with the peak of the inversion above 0°C (Fig. 8b). The mean temperature values profile indicates a mixed phase precipitation type as the surface was slightly above 0°C and the precipitation was experiencing sublimation or melting and evaporation prior to reaching the surface. Furthermore, the likely frontal inversion was also evident in the θ_e vertical profile and was nearly isentropic with height between 700 and 300 hPa (Fig. 8c). However, it should be noted that the mean values within the vertical profiles were not associated with an individual profile; therefore, in-depth quantitative analysis (i.e., instabilities) were not performed using the mean derived profile. To address this, the 18 UTC 11 April 2019 radiosonde from the Minneapolis/St. Paul, Minnesota was examined (dashed lines; Fig. 8). The National Weather Service launched this special 18 UTC upper air sounding to provide situational awareness as the snowstorm began to dissipate. At that time, Minneapolis/St. Paul were along the edge of the of dry slot and the precipitation band. The surface-based CAPE, MU-CAPE, and mid-level (700-500 hPa) lapse rates were calculated via MetPy (May et al., 2022). The mid-level (700-500 hPa) lapse rate was 7.5 C km^{-1}, with CAPE and MU-CAPE values of 0 J kg^{-1} and 268.8J kg^{-1}, respectively (Fig. 8b). This suggests that the environment for this thundersnow outbreak case was conditionally unstable with higher potential for elevated convection.

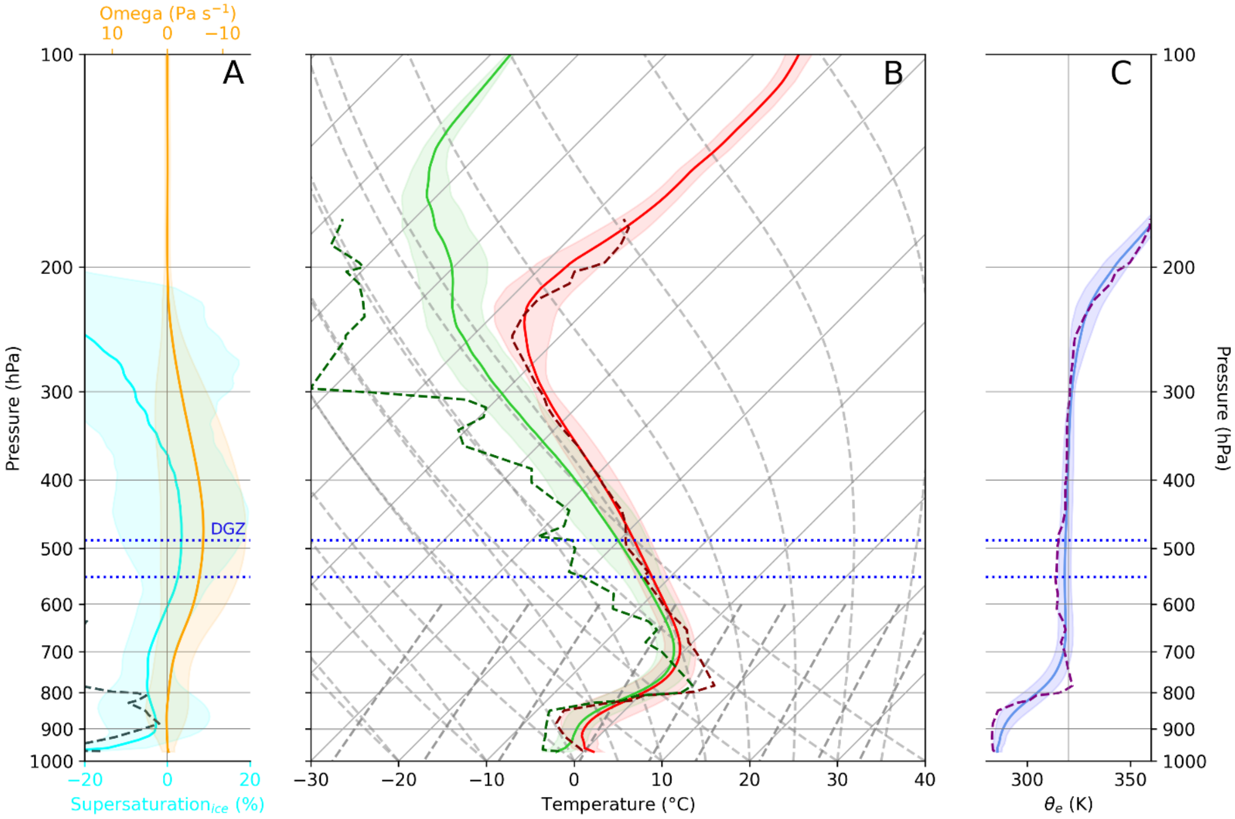

Figure 8: Mean vertical profiles (solid line) and associated standard deviation (shaded) for 1,733 simulated thundersnow flashes. The blue dotted blue line indicates the mean simulated dendritic growth zone. A) vertical motions (orange) and ice supersaturation (cyan); B) temperature (red) and dew point temperature (green); and C) equivalent potential temperature (blue). The dashed lines

in each of the panels represents observed data from the 18 UTC 11 April 2019 Minneapolis/St. Paul, Minnesota radiosonde.

4 Discussion

Figure 4 (and Supplemental Material 3) demonstrate the separation of the largest reflectivities in the main synoptic snowband and the occurrence of thundersnow. Interestingly, these also potentially show why thundersnow does not occur in the heaviest surface snowfall rates or the largest reflectivities (Harkema et al., 2020; Market & Becker, 2009). NU-WRF-ELEC suggested that the heavy-banded snowfall structure was associated with near homogeneous charge sign structure in the vertical. NU-WRF-ELEC indicated negative charge at x=350 and positive charge at x=400 from the surface to ~7 km AGL. There is no strong vertical charge separation; hence, no lightning initiation points within the heavy-banded snowfall structure. Supplemental Material 4 displays cross-sections of the total, snow, ice, and graupel charge density at 0710 UTC on 11 April 2019. The large positive region at x=400 consisted of positive snow charge density with lower ice and graupel negative charge density magnitudes. At x=350, the snow, ice, and graupel hydrometeors were all negatively charged. As a result, no appreciable vertical charge separation was evident but, rather, a horizontal gradient of charge; particularly associated with snow. Sedimentation brings these positively charged hydrometeors toward the surface and, thus, yields to this horizontal gradient in snow charge densities (Supplemental Material 5). Furthermore, it was determined that WRF-ELEC indicated that zero charging (i.e., non-inductive and inductive) was evident within the vertically homogeneous charge regions within the largest reflectivities of the synoptic snowband (Supplemental Material 6). However, it should be noted that WRF-ELEC has a minimum rime accretion rate (i.e., 0.1 g m^{-2} s^{-1}) regarding charging. In other words, the rime rate must exceed this minimum threshold for WRF-ELEC to calculate any noninductive charging. This could suggest that the non-inductive charging mechanism within non-riming environments (e.g., Dye & Bansemer, 2019; Dye & Willett, 2007; Harkema et al., 2023) may play a role in charge generation within synoptic snowbands. WRF-ELEC cannot explicitly back this up, but it is a fair assumption given that hydrometeors collisions were expected within the region of interest.

The large reflectivities within the main snowband are associated with a reduction of snow hydrometeor concentration which indicates aggregation. Mid-level frontogenesis induces a thermal circulation associated with downward advection on the northern extent of the circulation. The thermal circulation likely retained these positively charge particles aloft, in part, until the isentropic motions transported the snow particles toward the northern extent of the mid-level frontogenesis. The circulation transitioned into downdrafts forcing the positively charged snow particles down to the surface. As a result, a horizontal juxtaposition of negatively and positively charged snow hydrometeors ensues that potentially accounts for the spatial separation of thundersnow events from the heaviest reflectivities/snowfall rates. Figure 9 displays a conceptual model of this process based on the NU-WRF-ELEC simulation output. Going from right to left in Figure 9, the vertical air motion in the developing convective cells exceeds the snow fall speed, retaining it aloft until its terminal fall speeds exceed updraft speeds; leading ultimately to increased surface snowfall rates. The lofting and advection of snowfall via the thermal circulation induced by mid-level frontogenesis documented herein is consistent with Lackmann & Thompson, (2019). They determined that lofting increases snowfall homogeneity within the synoptic snowband structure; which is evident by the horizontal and vertical snow charge distribution within the same region (Fig. 4; Supplemental Material 5). It should be noted that particle motion is a combination of vertical air motion and terminal fall speed.

The rightmost positive charge region below the frontogenesis is associated with graupel; rebounding collisions between graupel and ice/snow hydrometeors leaves graupel pellets with a net positive charge, documented in Supplemental Material 4 (e.g., Jayaratne et al., 1983; Takahashi et al., 1999). Graupel will precipitate to the surface sooner while the ice/snow hydrometeors will sediment further downstream from the charging location (i.e., north of the graupel in this case). It should be noted that graupel concentrations were relatively low (i.e., < 1 kg^{-1}) within the cross-section at 0710 UTC on 11 April 2019 (Supplemental Material 4c). These still played a major role in electrification processes as evidenced by the large graupel charge densities. This analysis consists of a single case and additional cases should be examined for comparison as well as potential consistency between Midwest cyclones and Nor'easters**.**

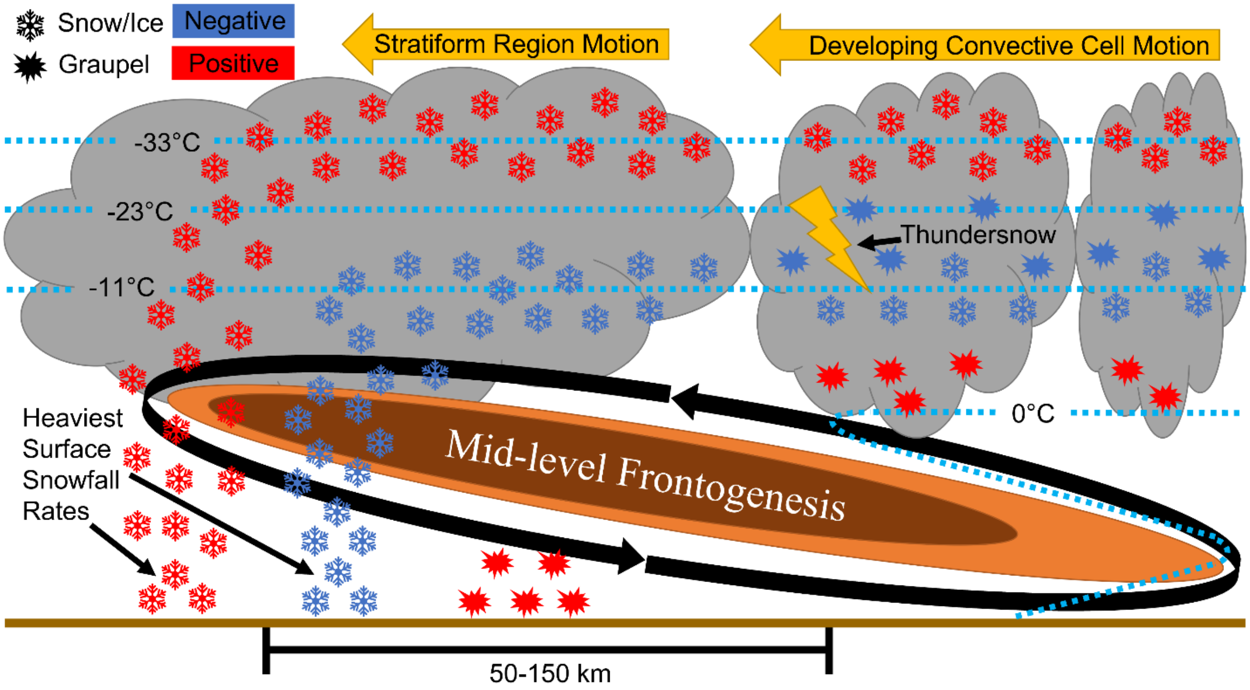

Figure 9: Conceptual model linking mid-level frontogenesis induced thermal circulation with the spatial separation of thundersnow and the horizontal separation between charged snow hydrometeors within the main synoptic snowband. The coloration of the hydrometeor symbols indicates hydrometeor charge polarity.

Previous studies have simulated **E** in winter storms (e.g., Dafis et al., 2018; Fierro et al., 2013; Harkema et al., 2023) but as far as the authors are aware no study has targeted their effort in simulating thundersnow events using WRF-ELEC. As a result, this study should be considered as an initial effort to simulate thundersnow flashes that were spatially aligned with observed thundersnow flashes (Fig. 6). Despite this success, the NU-WRF-ELEC simulation herein does not capture the full extent of the geographical region that experiences thundersnow nor the magnitude of total thundersnow flash rates when compared to GLM. When comparing all the lightning flashes within the NU-WRF-ELEC model output, the total (thundersnow + non thundersnow) simulated FED magnitude and spatial coverage increases and aligns slightly better with GLM observations (Supplemental Material 7). This suggests that the definition of thundersnow within the simulation (i.e., $T_w \leq 2°C$ & $T \leq 2°C$) might not be capturing the true extent of thundersnow within the model. Another possible culprit in the spatial and magnitude differences between the simulation and observations is that NU-WRF-ELEC does not simulate tower-initiated flashes, which could account for 10-30% of thundersnow flashes (Harkema et al., 2019; Schultz et al., 2018). Additionally, it is likely that NU-WRF-ELEC produced less thundersnow compared to observations as the model could not fundamentally resolve all key cloud-scale microphysics and electrification processes that were occurring in the event. Within the inner-domain of the NU-WRF-ELEC simulation, the NSSL microphysics scheme did not adequately parameterize the microphysical processes that were found within the wintertime stratiform/convective region that ultimately led to the event being a thundersnow outbreak case. A deep dive into each of the above would be necessary to specifically determine which one had the most impact regarding the underperformance in thundersnow initiation in the simulation. However, such an endeavor is well beyond the scope of the project.

The simulated thundersnow flash sizes were drastically smaller compared to the GLM observations and is best seen in Supplemental Material 1. These differences come from the inherent differences between the WRF-ELEC parameterization and GLM. First and foremost, WRF-ELEC struggled to simulate the larger in-frequent thundersnow flashes throughout the event (e.g., Wisconsin; Fig. 6). WRF-ELEC bounds the lightning volume channel by values of the electric potential at each channel end. This likely inhibited WRF-ELEC from producing larger thundersnow flashes and prevented the discharge scheme from neutralizing ample charge. It is also worth noting that it is unknown how a CG flash is determined in the lightning parameterization (as it is a newer addition to WRF-ELEC) and it is likely not optimized, particularly for winter cases. Additionally, the charging rates within stratiform regions may not be well represented within the simulation. Furthermore, GLM is an optical sensor that has a native grid spacing of ~8km at nadir. Lightning does not need to propagate throughout an entire ~64 km^2 GLM pixel to be classified as lightning but simply needs to exceed an optical emission threshold. As a result, GLM could overestimate the spatial coverage of thundersnow flashes compared to the extent of the flash observed by other systems (e.g., lightning mapping arrays; Schultz et al. 2018).

5 Conclusions

The 10-12 April 2019 thundersnow outbreak that occurred in the northern Great Plains was examined via observations and simulated using numerical model with explicit electrification parameterizations (i.e., NU-WRF-ELEC). Observed NLDN thundersnow flashes were examined via MRMS isothermal and 3-D reflectivities. More specifically, the median isothermal reflectivity values were found to be 29.0 and 26.5 dBZ at -10°C and -20°C, respectively. The mode values were ~3 dBZ lower compared to the median values. Thundersnow flashes (N=1,733) were simulated using WRF-ELEC and occurred within elevated convection that traversed along mid-level frontogenesis via isentropic lift. The simulated charge densities indicated a gross tripole charge structure with ice/snow hydrometeors contributing most to the lower portion of the negative charge region (and negative graupel to the upper part). Positively charged ice/snow hydrometeors formed the upper positive charge region in a mixture with negatively charged graupel. When compared to observed thundersnow flashes, NU-WRF-ELEC was able to produce thundersnow but underestimated the spatial extent and magnitude of the observed thundersnow flashes from GLM. Simulated thundersnow flashes were also smaller than the observed flashes. These discrepancies could be partly a result of different definitions of thundersnow between the simulation (i.e., T_w and $T \leq 2°C$) and observations (i.e., overlap of GLM and derived surface snowfall rates), and the lack of tower-initiated flashes in NU-WRF-ELEC, which can account for 10-30% of observed thundersnow flashes. The most likely explanation for the large discrepancy between thundersnow in the simulation and observations was that the simulation did not adequately parameterize the in-cloud microphysical and/or electrification processes that led to the large-scale thundersnow outbreak. The Minneapolis/St. Paul radiosonde from 18 UTC 11 April 2019 indicated that the environment was conditional unstable and supportive of elevated convection and aligns with previous studies (e.g., Market et al., 2006). Lastly, it was hypothesized that thundersnow initiation was spatially displaced from the largest reflectivities within the synoptic snowband because of the thermal circulation – induced by mid-level frontogenesis – advecting positively charged ice/snow hydrometeors down towards the surface (Fig. 9). This advection led to a nearly homogeneous vertical structure in charge sign within the simulated synoptic snowband with charge gradients being more prevalent in the horizontal rather than the vertical (see Supplemental Material 3,5).

To the authors' knowledge, this study represents a first effort in successfully simulated thundersnow events using WRF-ELEC. Despite this success, the number of simulated flashes was substantially less than what was observed from space- and ground-based lightning detection networks. Given that the NSSL microphysical scheme exhibits a bias towards stronger aggregation, it would be desired to adjust in future work the aggregation parameterization to better match with the observations. Another plausible research route would be to approach the case with different parameterization configurations and boundary conditions. This would resemble an ensemble simulation and provide additional insight into which configuration/ensemble provides the best representation of the lightning observations (along with some estimation of uncertainty). This study also developed a simple conceptual model to potentially explain why thundersnow initiation is horizontally separated from the heaviest snowfall rates within the synoptic snowband; however, this conceptual model needs to be tested against cases that contain thundersnow and those that do not.

Acknowledgments

This work is part of a larger investigation of electrified snowfall that is directly supported through NASA's Future Investigators in NASA Earth and Space Science and Technology (FINESST) program # 80NSSC20K1623. Additionally, this work was also supported by Dr. Tsengdar Lee of NASA's Research and Analysis Program, Weather and Atmospheric Dynamics Focus Area, as part of the Short-term Prediction Research and Transition (SPoRT) Center at Marshall Space Flight Center and supported through the NASA-UAH Cooperative agreement # 80MSFC22M0004. The authors would also like to thank the NASA Center for Climate Simulation for allotting computational time on the Discover Supercomputer to run the NU-WRF-ELEC simulation. The authors would also like to thank Dr. Kwo-Sen Kuo of NASA GFSC for providing access to the MRMS data. Lastly, the authors want to thank the three anonymous reviewers for providing critical insight and suggestions.

Open Research

The HRRR data used to initialize the NU-WRF-ELEC simulation can be obtained via NOAA's Amazon Web Service (accessed via https://noaa-hrrr-bdp-pds.s3.amazonaws.com/index.html). NU-WRF-ELEC software are available in https://nuwrf.gsfc.nasa.gov/software. Observed radiosonde data are available from the University of Wyoming (http://weather.uwyo.edu/upperair/sounding.html). National Operational Hydrologic Remote Sensing Center snowfall accumulation data are available at https://www.nohrsc.noaa.gov/snowfall_v2/. The GLM data used in this work are available from Amazon S3 buckets through Amazon Web Services: https://registry.opendata.aws/noaa-goes/. ENTLN and NLDN data can be accessed via Earth Networks (https://www.earthnetworks.com/product/lightning-data/) and Vaisala (https://www.vaisala.com/en/products/national-lightning-detection-network-nldn), respectively. MRMS data that were used in this study are available (see Harkema et al. 2024).

References

Adhikari, A., & Liu, C. (2019). Geographical Distribution of Thundersnow Events and Their Properties From GPM Ku-Band Radar. *Journal of Geophysical Research: Atmospheres*, *124*(4), 2031–2048. https://doi.org/10.1029/2018JD028839

Benjamin, S. G., Weygandt, S. S., Brown, J. M., Hu, M., Alexander, C. R., Smirnova, T. G., et al. (2016). A North American Hourly Assimilation and Model Forecast Cycle: The Rapid Refresh. *Monthly Weather Review*, *144*(4), 1669–1694. https://doi.org/10.1175/MWR-D-15-0242.1

Bruning, E. C., Tillier, C. E., Edgington, S. F., Rudlosky, S. D., Zajic, J., Gravelle, C., et al. (2019). Meteorological Imagery for the Geostationary Lightning Mapper. *Journal of Geophysical Research: Atmospheres*, *124*(24), 14285–14309. https://doi.org/10.1029/2019JD030874

Chiu, C.-S. (1978). Numerical study of cloud electrification in an axisymmetric, time-dependent cloud model. *Journal of Geophysical Research: Oceans*, *83*(C10), 5025–5049. https://doi.org/10.1029/JC083iC10p05025

Cummins, K. L., & Murphy, M. J. (2009). An Overview of Lightning Locating Systems: History, Techniques, and Data Uses, With an In-Depth Look at the U.S. NLDN. *IEEE Transactions on Electromagnetic Compatibility*, *51*(3), 499–518. https://doi.org/10.1109/TEMC.2009.2023450

Curran, J. T., & Pearson, A. D. (1971). *Proximity Soundings for Thunderstorms with Snow*. Presented at the American Meteorological Society, Kansas City, MO.

Dafis, S., Fierro, A., Giannaros, T. M., Kotroni, V., Lagouvardos, K., & Mansell, E. (2018). Performance Evaluation of an Explicit Lightning Forecasting System. *Journal of Geophysical Research: Atmospheres*, *123*(10), 5130–5148. https://doi.org/10.1029/2017JD027930

Dwyer, J. R. (2003). A fundamental limit on electric fields in air. *Geophysical Research Letters*, *30*(20). https://doi.org/10.1029/2003GL017781

Dye, J. E., & Bansemer, A. (2019). Electrification in Mesoscale Updrafts of Deep Stratiform and Anvil Clouds in Florida. *Journal of Geophysical Research: Atmospheres*, *124*(2), 1021–1049. https://doi.org/10.1029/2018JD029130

Dye, J. E., & Willett, J. C. (2007). Observed Enhancement of Reflectivity and the Electric Field in Long-Lived Florida Anvils. *Monthly Weather Review*, *135*(10), 3362–3380. https://doi.org/10.1175/MWR3484.1

Ek, M. B., Mitchell, K. E., Lin, Y., Rogers, E., Grunmann, P., Koren, V., et al. (2003). Implementation of Noah land surface model advances in the National Centers for

Environmental Prediction operational mesoscale Eta model. *Journal of Geophysical Research: Atmospheres*, *108*(D22). https://doi.org/10.1029/2002JD003296

Fierro, A. O., Mansell, E. R., MacGorman, D. R., & Ziegler, C. L. (2013). The Implementation of an Explicit Charging and Discharge Lightning Scheme within the WRF-ARW Model: Benchmark Simulations of a Continental Squall Line, a Tropical Cyclone, and a Winter Storm. *Monthly Weather Review*, *141*(7), 2390–2415. https://doi.org/10.1175/MWR-D-12-00278.1

Fierro, A. O., Mansell, E. R., Ziegler, C. L., & MacGorman, D. R. (2015). Explicitly Simulated Electrification and Lightning within a Tropical Cyclone Based on the Environment of Hurricane Isaac (2012). *Journal of the Atmospheric Sciences*, *72*(11), 4167–4193. https://doi.org/10.1175/JAS-D-14-0374.1

Goodman, S. J., Blakeslee, R. J., Koshak, W. J., Mach, D., Bailey, J., Buechler, D., et al. (2013). The GOES-R Geostationary Lightning Mapper (GLM). *Atmospheric Research*, *125–126*, 34–49. https://doi.org/10.1016/j.atmosres.2013.01.006

Harkema, S. S., Schultz, C. J., Berndt, E. B., & Bitzer, P. M. (2019). Geostationary Lightning Mapper Flash Characteristics of Electrified Snowfall Events. *Weather and Forecasting*, *34*(5), 1571–1585. https://doi.org/10.1175/WAF-D-19-0082.1

Harkema, S. S., Berndt, E. B., & Schultz, C. J. (2020). Characterization of Snowfall Rates, Totals, and Snow-to-Liquid Ratios in Electrified Snowfall Events Identified by the Geostationary Lightning Mapper. *Weather and Forecasting*, *35*(2), 673–689. https://doi.org/10.1175/WAF-D-19-0126.1

Harkema, S. S., Berndt, E. B., Mecikalski, J. R., & Cordak, A. (2022). Advanced Baseline Imager Cloud-Top Trajectories and Properties of Electrified Snowfall Flash Initiation. *Weather and Forecasting*, *36*(6), 2289–2303. https://doi.org/10.1175/WAF-D-21-0003.1

Harkema, S. S., Carey, L. D., Schultz, C. J., Mansell, E. R., Berndt, E. B., Fierro, A. O., & Matsui, T. (2023). Electrification Within Wintertime Stratiform Regions Sampled During the 2020/2022 NASA IMPACTS Field Campaign. *Journal of Geophysical Research: Atmospheres*, *128*(18), e2023JD038708. https://doi.org/10.1029/2023JD038708

Harkema, S.S., Mansell, E. R., Fierro, A. O., Carey, L. D., Schultz, C. J., Masui, T., & Berndt, E. B., (2024). 11 April 2019 MRMS Data Subset for Harkema et al. (2024) [Dataset]. Zenodo. https://doi.org/10.5281/zenodo.10849031.

Iacono, M. J., Delamere, J. S., Mlawer, E. J., Shephard, M. W., Clough, S. A., & Collins, W. D. (2008). Radiative forcing by long-lived greenhouse gases: Calculations with the AER radiative transfer models. *Journal of Geophysical Research: Atmospheres*, *113*(D13). https://doi.org/10.1029/2008JD009944

Jayaratne, E. R., Saunders, C. P. R., & Hallett, J. (1983). Laboratory studies of the charging of soft-hail during ice crystal interactions. *Quarterly Journal of the Royal Meteorological Society*, *109*(461), 609–630. https://doi.org/10.1002/qj.49710946111

Kain, J. S., Weiss, S. J., Levit, J. J., Baldwin, M. E., & Bright, D. R. (2006). Examination of Convection-Allowing Configurations of the WRF Model for the Prediction of Severe Convective Weather: The SPC/NSSL Spring Program 2004. *Weather and Forecasting*, *21*(2), 167–181. https://doi.org/10.1175/WAF906.1

Kitagawa, N., & Michimoto, K. (1994). Meteorological and electrical aspects of winter thunderclouds. *Journal of Geophysical Research: Atmospheres*, *99*(D5), 10713–10721. https://doi.org/10.1029/94JD00288

Krehbiel, P. R. (1986). *The Electrical Struture of Thunderstorms*. National Academy Press.

Kumjian, M. R., & Deierling, W. (2015). Analysis of Thundersnow Storms over Northern Colorado. *Weather and Forecasting*, *30*(6), 1469–1490. https://doi.org/10.1175/WAF-D-15-0007.1

Lackmann, G. M., & Thompson, G. (2019). Hydrometeor Lofting and Mesoscale Snowbands. *Monthly Weather Review*, *147*(11), 3879–3899. https://doi.org/10.1175/MWR-D-19-0036.1

Lang, S. E., Tao, W.-K., Chern, J.-D., Wu, D., & Li, X. (2014). Benefits of a Fourth Ice Class in the Simulated Radar Reflectivities of Convective Systems Using a Bulk Microphysics Scheme. *Journal of the Atmospheric Sciences*, *71*(10), 3583–3612. https://doi.org/10.1175/JAS-D-13-0330.1

Liu, C., & Heckman, S. (2010). *The Application of Total Lightning Detection and Cell Tracking for Severe Weather Prediction*. Presented at the TECO-2010-WMO Tech. Conf. on Meteorological and Environmental Instruments and Methods of Observation, Helsinki, Finland. Retrieved from https://www.wmo.int/pages/prog/www/IMOP/publications/IOM-104_TECO-2010/P2_7_Heckman_USA.pdf.

Lyons, W. A., Bruning, E. C., Warner, T. A., MacGorman, D. R., Edgington, S., Tillier, C., & Mlynarczyk, J. (2020). Megaflashes: Just How Long Can a Lightning Discharge Get? *Bulletin of the American Meteorological Society*, *101*(1), E73–E86. https://doi.org/10.1175/BAMS-D-19-0033.1

MacGorman, D. R., Straka, J. M., & Ziegler, C. L. (2001). A Lightning Parameterization for Numerical Cloud Models. *Journal of Applied Meteorology and Climatology*, *40*(3), 459–478. https://doi.org/10.1175/1520-0450(2001)040<0459:ALPFNC>2.0.CO;2

Mansell, E. R., MacGorman, D. R., Ziegler, C. L., & Straka, J. M. (2005). Charge structure and lightning sensitivity in a simulated multicell thunderstorm. *Journal of Geophysical Research: Atmospheres*, *110*(D12). https://doi.org/10.1029/2004JD005287

Mansell, E. R., Ziegler, C. L., & Bruning, E. C. (2010). Simulated Electrification of a Small Thunderstorm with Two-Moment Bulk Microphysics. *Journal of the Atmospheric Sciences*, *67*(1), 171–194. https://doi.org/10.1175/2009JAS2965.1

Market, P. S., & Becker, A. E. (2009). A study of lightning flashes attending periods of banded snowfall. *Geophysical Research Letters*, *36*(1). https://doi.org/10.1029/2008GL036317

Market, P. S., Oravetz, A. M., Gaede, D., Bookbinder, E., Lupo, A. R., Melick, C. J., et al. (2006). Proximity soundings of thundersnow in the central United States. *Journal of Geophysical Research: Atmospheres*, *111*(D19). https://doi.org/10.1029/2006JD007061

May, R. M., Goebbert, K. H., Thielen, J. E., Leeman, J. R., Camron, M. D., Bruick, Z., et al. (2022). MetPy: A Meteorological Python Library for Data Analysis and Visualization. *Bulletin of the American Meteorological Society*, *103*(10), E2273–E2284. https://doi.org/10.1175/BAMS-D-21-0125.1

McMurdie, L. A., Heymsfield, G. M., Yorks, J. E., Braun, S. A., Skofronick-Jackson, G., Rauber, R. M., et al. (2022). Chasing Snowstorms: The Investigation of Microphysics and Precipitation for Atlantic Coast-Threatening Snowstorms (IMPACTS) Campaign. *Bulletin of the American Meteorological Society*, *103*(5), E1243–E1269. https://doi.org/10.1175/BAMS-D-20-0246.1

Meng, H., Dong, J., Ferraro, R., Yan, B., Zhao, L., Kongoli, C., et al. (2017). A 1DVAR-based snowfall rate retrieval algorithm for passive microwave radiometers. *Journal of Geophysical Research: Atmospheres*, *122*(12), 6520–6540. https://doi.org/10.1002/2016JD026325

Meng, H., Dong, J., Kongoli, C., Ferraro, R., Yan, B., White, K., et al. (2017). *NESDIS Snowfall Rate Product and its Applications*. JPSS Science Seminar. Retrieved from http://www. jpss.noaa.gov/assets/pdfs/science_seminars/presentations/Snowfall Rate_Meng_White_Berndt_2017.pdf

Mosier, R. M., Schumacher, C., Orville, R. E., & Carey, L. D. (2011). Radar Nowcasting of Cloud-to-Ground Lightning over Houston, Texas. *Weather and Forecasting*, *26*(2), 199–212. https://doi.org/10.1175/2010WAF2222431.1

Nicholls, S. D., Decker, S. G., Tao, W.-K., Lang, S. E., Shi, J. J., & Mohr, K. I. (2017). Influence of bulk microphysics schemes upon Weather Research and Forecasting (WRF) version 3.6.1 nor'easter simulations. *Geoscientific Model Development*, *10*(2), 1033–1049. https://doi.org/10.5194/gmd-10-1033-2017

Noh, Y., Cheon, W. G., Hong, S. Y., & Raasch, S. (2003). Improvement of the K-profile Model for the Planetary Boundary Layer based on Large Eddy Simulation Data. *Boundary-Layer Meteorology*, *107*(2), 401–427. https://doi.org/10.1023/A:1022146015946

Peters-Lidard, C. D., Kemp, E. M., Matsui, T., Santanello, J. A., Kumar, S. V., Jacob, J. P., et al. (2015). Integrated modeling of aerosol, cloud, precipitation and land processes at satellite-resolved scales. *Environmental Modelling & Software*, *67*, 149–159. https://doi.org/10.1016/j.envsoft.2015.01.007

Rauber, R. M., Wegman, J., Plummer, D. M., Rosenow, A. A., Peterson, M., McFarquhar, G. M., et al. (2014). Stability and Charging Characteristics of the Comma Head Region of Continental Winter Cyclones. *Journal of the Atmospheric Sciences*, *71*(5), 1559–1582. https://doi.org/10.1175/JAS-D-13-0253.1

Reynolds, S. E., Brook, M., & Gourley, M. F. (1957). THUNDERSTORM CHARGE SEPARATION. *Journal of the Atmospheric Sciences*, *14*(5), 426–436. https://doi.org/10.1175/1520-0469(1957)014<0426:TCS>2.0.CO;2

Rudlosky, S. D., & Virts, K. S. (2021). Dual Geostationary Lightning Mapper Observations. *Monthly Weather Review*, *149*(4), 979–998. https://doi.org/10.1175/MWR-D-20-0242.1

Rudlosky, S. D., Goodman, S. J., Virts, K. S., & Bruning, E. C. (2019). Initial Geostationary Lightning Mapper Observations. *Geophysical Research Letters*, *46*(2), 1097–1104. https://doi.org/10.1029/2018GL081052

Rust, W. D., & Trapp, R. J. (2002). Initial balloon soundings of the electric field in winter nimbostratus clouds in the USA. *Geophysical Research Letters*, *29*(20), 20-1-20–4. https://doi.org/10.1029/2002GL015278

Saunders, C. P. R., & Peck, S. L. (1998). Laboratory studies of the influence of the rime accretion rate on charge transfer during crystal/graupel collisions. *Journal of Geophysical Research: Atmospheres*, *103*(D12), 13949–13956. https://doi.org/10.1029/97JD02644

Saunders, C. P. R., Bax-norman, H., Emersic, C., Avila, E. E., & Castellano, N. E. (2006). Laboratory studies of the effect of cloud conditions on graupel/crystal charge transfer in thunderstorm electrification. *Quarterly Journal of the Royal Meteorological Society*, *132*(621), 2653–2673. https://doi.org/10.1256/qj.05.218

Schultz, C. J., Lang, T. J., Bruning, E. C., Calhoun, K. M., Harkema, S., & Curtis, N. (2018). Characteristics of Lightning Within Electrified Snowfall Events Using Lightning Mapping Arrays. *Journal of Geophysical Research: Atmospheres*, *123*(4), 2347–2367. https://doi.org/10.1002/2017JD027821

Schultz, C. J., Harkema, S. S., Mach, D. M., Bateman, M., Lang, T. J., Heymsfield, G. M., et al. (2021). Remote Sensing of Electric Fields Observed Within Winter Precipitation During the 2020 Investigation of Microphysics and Precipitation for Atlantic Coast-Threatening Snowstorms (IMPACTS) Field Campaign. *Journal of Geophysical Research: Atmospheres*, *126*(16), e2021JD034704. https://doi.org/10.1029/2021JD034704

Seroka, G. N., Orville, R. E., & Schumacher, C. (2012). Radar Nowcasting of Total Lightning over the Kennedy Space Center. *Weather and Forecasting*, *27*(1), 189–204. https://doi.org/10.1175/WAF-D-11-00035.1

Skamarock, W., & Klemp, J. (2008). A time-split nonhydrostatic atmospheric model for weather research and forecasting applications. *J. Comput. Phys.* https://doi.org/10.1016/j.jcp.2007.01.037

Smith, T. M., Lakshmanan, V., Stumpf, G. J., Ortega, K. L., Hondl, K., Cooper, K., et al. (2016). Multi-Radar Multi-Sensor (MRMS) Severe Weather and Aviation Products: Initial Operating Capabilities. *Bulletin of the American Meteorological Society*, *97*(9), 1617–1630. https://doi.org/10.1175/BAMS-D-14-00173.1

Stith, J. L., Dye, J. E., Bansemer, A., Heymsfield, A. J., Grainger, C. A., Petersen, W. A., & Cifelli, R. (2002). Microphysical Observations of Tropical Clouds. *Journal of Applied Meteorology and Climatology*, *41*(2), 97–117. https://doi.org/10.1175/1520-0450(2002)041<0097:MOOTC>2.0.CO;2

Takahashi, T. (1978). Riming Electrification as a Charge Generation Mechanism in Thunderstorms. *Journal of the Atmospheric Sciences*, *35*(8), 1536–1548. https://doi.org/10.1175/1520-0469(1978)035<1536:REAACG>2.0.CO;2

Takahashi, T., Tajiri, T., & Sonoi, Y. (1999). Charges on Graupel and Snow Crystals and the Electrical Structure of Winter Thunderstorms. *Journal of the Atmospheric Sciences*, *56*(11), 1561–1578. https://doi.org/10.1175/1520-0469(1999)056<1561:COGASC>2.0.CO;2

Williams, E. R. (1989). The tripole structure of thunderstorms. *Journal of Geophysical Research: Atmospheres*, *94*(D11), 13151–13167. https://doi.org/10.1029/JD094iD11p13151

Yuter, S. E., & Houze, R. A. (1995). Three-Dimensional Kinematic and Microphysical Evolution of Florida Cumulonimbus. Part II: Frequency Distributions of Vertical Velocity, Reflectivity, and Differential Reflectivity. *Monthly Weather Review*, *123*(7), 1941–1963. https://doi.org/10.1175/1520-0493(1995)123<1941:TDKAME>2.0.CO;2

Ziegler, C. L., & MacGorman, D. R. (1994). Observed Lightning Morphology Relative to Modeled Space Charge and Electric Field Distributions in a Tornadic Storm. *Journal of the Atmospheric Sciences*, *51*(6), 833–851. https://doi.org/10.1175/1520-0469(1994)051<0833:OLMRTM>2.0.CO;2

Ziegler, C. L., MacGorman, D. R., Dye, J. E., & Ray, P. S. (1991). A model evaluation of noninductive graupel-ice charging in the early electrification of a mountain thunderstorm. *Journal of Geophysical Research: Atmospheres*, *96*(D7), 12833–12855. https://doi.org/10.1029/91JD01246